Identifying the Key Obstacle in Photocatalytic Oxygen Evolution on Rutile TiO_2

Dong Wang,[1]† Tian Sheng,[1]† Jianfu Chen,[1] Hai-Feng Wang,[1]* P. Hu[1,2]*

[1]Key Lab of Advanced Materials, Center for Computational Chemistry and Research Institute of Industrial Catalysis, East China University of Science and Technology, China

[2]School of Chemistry and Chemical Engineering, Queen's University Belfast, UK

* Corresponding authors: p.hu@qub.ac.uk; hfwang@ecust.edu.cn

† These authors contributed equally to this work.

Abstract

As the bottleneck in photocatalytic water splitting, the oxygen evolution reaction (OER) has drawn huge attention, but its efficiency still falls short of expectations. A widely accepted speculation is that the catalytic activity of catalysts is insufficient (high reaction barriers). Herein, we develop a first-principles method to investigate the photocatalytic OER at the water/TiO_2(110) interface. A full mechanism uncovering the importance of radicals is determined. Kinetic analysis further enables us to quantitatively estimate each possible obstacle in the process. We demonstrate unambiguously that the rate-determining factor of OER varies with the concentration of surface-reaching photoholes (C_{h+}). Under experimental conditions, the intrinsic catalytic activity of TiO_2(110) dose not represent the major obstacle, but all steps involving photoholes are slow due to their low concentrations. It suggests that the key to enhance the OER efficiency at the current stage (before approaching the estimated threshold C_{h+} = ~10^{-4}) is to increase C_{h+}.

Introduction

As an environmentally friendly approach to generate renewable energy directly from the sun, potentially achieving the sustainable energy development, photocatalytic water splitting ($H_2O \xrightarrow{h\nu} ½O_2 + H_2$) has drawn huge attention in chemistry[1,2]. Overall, this process consists of the hydrogen evolution reaction ($H^+ + e^- \rightarrow ½H_2$) and the oxygen evolution reaction with photoholes h^+ involved (OER: $2H_2O + 4h^+ \rightarrow O_2 + 4H^+$) (Fig. 1a), among which the OER is known to be the bottleneck in photocatalytic water splitting, hindering the overall process[3]. Therefore, huge efforts

have been made to increase the efficiency of OER on a variety of catalysts, especially on TiO_2 which is perhaps one of the most important materials in photocatalysis due to its natural abundance, cheap price, non-toxicity and superior photostability[2,3].

Amongst different extensively studied topics, the reaction mechanism of OER has been the main focus both experimentally and theoretically. It is anticipated that further insight into the mechanism can provide a guidance to rationally improve the catalytic efficiency. However, such studies fell short on their promises due to the complicated nature of OER and the limitations of approaches used. Based on the experimental work, mainly two mechanisms were suggested. It has long been speculated that O_2 is produced from H_2O_2 by coupling two surface ·OH radicals[4]. But later spectroscopy results excluded the generation of H_2O_2 in OER[5,6]. Subsequently, a nucleophilic attack mechanism was proposed, suggesting that the O-O bond is formed by the involvement of lattice O[5,7,8]. Theoretically, few studies were reported on the overall OER at the liquid/solid interface due to the difficulties in simulating surface radicals (trapped holes on surface) and aqueous environment. Most works were limited on the initial water dissociation step[9,10] with few exploratory studies focused on the thermodynamics of the process[11-13]. It is clear that due to the limitations in both experimental and theoretical approaches, the mechanism of OER remains elusive.

In addition to the mechanism, extensive investigations have also been carried out on a variety of other issues, such as the photocatalyst preparation[1,2], the band structure modification (*e.g.* ion doping[14-16]), increasing the efficiency of photo-induced charge separation (*e.g.* phase junction[17-19]) and lowering the reaction barriers (*e.g.* the water dissociation barrier[20,21]). It is clear that there is still a lack of understanding on the main obstacle in OER and therefore it is not surprising that the overall efficiency of OER is still very unsatisfactory. Obviously, the following fundamental questions need to be answered in order to make a breakthrough: Firstly, what is the favored reaction mechanism of photocatalytic OER? Secondly, which factor determines the overall efficiency? Thirdly, how can we further improve the efficiency?

In this work, we choose the most stable rutile TiO_2(110) surface as the model photocatalyst (Fig. 1a), considering that the rutile phase is generally good for water oxidation[22,23] compared to the anatase phase[24,25]. A systematic computational investigation into the photocatalytic OER mechanism at the water/TiO_2(110) interface is carried out, using extensive first-principles molecular dynamics (MD) simulations. A comprehensive picture of the whole chemical process, consisting of H_2O dissociation, the formation of active radical species, and O-O coupling reaction, is obtained. Based on the completed reaction mechanism and detailed microkinetic analyses, we demonstrate that under experimental conditions the intrinsic catalytic activity of TiO_2 is not the rate-determining factor that limits the overall efficiency of OER. It is shown clearly that the low concentration of surface-reaching holes is the main obstacle in the system.

Results

Development of the MPA-MD approach. Theoretically, it is extremely difficult to calculate the OER since one has to overcome two major issues. The first one is to

correctly locate the photo-induced surface radicals, which is a prerequisite to test a variety of pathways in OER. As pointed out by Cheng and Sprik, the error of the commonly used PBE functional for calculating radicals can be as large as 0.6 eV, but the problem can be solved by using hybrid functional calculations, such as HSE06[26]. However, HSE06 functional is too time-consuming for the OER systems, particularly in the presence of the liquid phase. In our previous work[27,28], we showed that DFT+U can yield similar structures as the HSE06 functional with reasonable energies (Supplementary Fig. 1 and Note 1). In this work, we first used DFT+U method to run MD simulations as well as the structure optimization of each MD snapshot, and then all the selected samples from each MD simulation were further optimized/checked by the HSE06 functional. On using this technique, almost insurmountable hybrid functional calculations in this project could be carried out with a reasonable time scale; without this approach, it is perhaps impossible to test a variety of OER pathways as we did in the current work.

The second issue is to reliably calculate the reactions occurring at the liquid/solid interface. The explicit involvement of water environment is known to be important on the reaction energetics[29,30], which is also a prerequisite to investigate the proton transfer process commonly occurred at the liquid/solid interface. But there is no robust method for such systems using density functional theory (DFT) approaches. To calculate the OER reactions with good accuracy at the water/TiO_2 interface (Fig. 1a), we developed a general method, the so-called multi-point averaging molecular dynamics (MPA-MD): Firstly, we performed the normal MD calculations (~9 ps; Methods) of each intermediate state (IMS; including transition states) on TiO_2 (110) with the aqueous network above the surface. Secondly, in the MD simulation of each IMS, we selected a structure every 0.2 ps from the stabilized MD simulations (small fluctuation in energy after long simulations) and further optimized it to obtain the total energy of each structure (E_{tot}) at the HSE06 level. For each IMS, around 15 samples from the late part of each overall MD simulation (~3 ps) were obtained. Considering that different solution configuration of water network affects E_{tot}, we deducted the contribution of water solution in E_{tot} but keep the solvation effect into consideration for each sample as follows: (i) calculate the total energy of water solution (E_{water}) with exactly the same structure as in the optimized samples at the HSE06 level; (ii) deduct E_{water} from E_{tot} to obtain the solvation-included energy. Finally, we averaged the obtained solvation-included energies of all the samples in each IMS (more details on the MPA-MD method are provided in Supplementary Note 2).

Table 1 | Comparison of reaction barriers using different methods

Reactions in Solutions	E_a^1/eV [a]	E_a^2/eV [b]
$Pt(NH_3)_2Cl_2 + H_2O \rightarrow Pt(NH_3)_2Cl(H_2O)^+ + Cl^-$	0.78	0.75(exp. 0.84-1.07)[31]
$Na_nCl_n \rightarrow Na_nCl_{n-1}^+ + Cl^-$	0.15	0.11[32]
$O_2 \rightarrow 2O^*$ on Pt(111)	0.43	0.39
$O_2 + H^* \rightarrow OOH^*$ on Pt(111)	0.60	0.58
$H_2O^* \rightarrow OH^- + H^+$ on TiO_2 rutile (110)	0.51	0.54

Reaction barriers are computed using two methods, [a] our MPA-MD method and [b] the constrained MD method, in the presence of water solvents.

This method allows us to calculate all the elementary steps in the presence of liquid phase with good accuracy. Thorough tests on the reaction energetics including barriers were carried out to verify the reliability of our approach in dealing with aqueous systems. Five kinds of aqueous reactions were compared between our approach and the state-of-the-art constrained MD methods (Table 1; Methods), which, however, would be too time-consuming to use the constrained MD approach for the water/TiO_2(110) systems. As shown in Table 1, in all the cases our MPA-MD method gives very similar results to those from the constrained MD method. In particular, the comparable results of water dissociation (0.51 *vs.* 0.54 eV) as well as the good accuracy in estimating the point of zero charge (PZC; Supplementary Note 4) of rutile (110) surface (5.83 *vs.* exp. 5.5-4.8[33]) further manifest the feasibility of our method in investigating the OER mechanism at the aqueous/TiO_2(110) interface. We should point out that without our novel approach it is impossible to investigate the OER mechanism in such details as we did using first principles calculations.

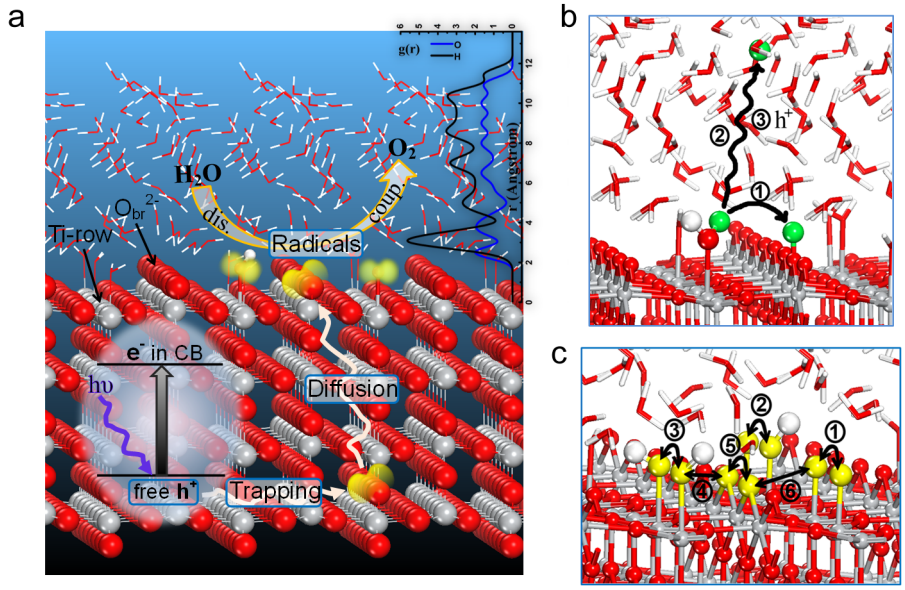

Fig. 1 | Schematic illustration of the photocatalytic OER at the water/TiO_2 interface. a, The general picture of OER. A four-Ti-layer $p(1\times4)$ periodical slab with 26 H_2O above the surface is used. Ti sites and bridge O are labeled and calculated densities of O and H in the water phase are shown in blue and black curves, respectively. **b**,**c**, Possible pathways of water dissociation (**b**) and OO coupling (**c**) among surface radicals (highlighted in yellow): (1) coupling between O_t^- and O_t^-; (2) $\cdot OH_t$ and O_t^-; (3) $\cdot OH_t$ and $\cdot OH_t$; (4) $\cdot OH_t$ and O_{br}^-; (5) O_{br}^- and O_{br}^-; (6) O_t^- and O_{br}^-. Grey: Ti; red: O; white: H. This colour notation is used throughout the paper.

The OER mechanism. The whole mechanism of OER can be broadly divided into two parts: The first part is the water dissociation and the formation of surface species, and the second one is the oxygen-oxygen bond formation, yielding O_2 (*i.e.* OO

coupling among surface species).

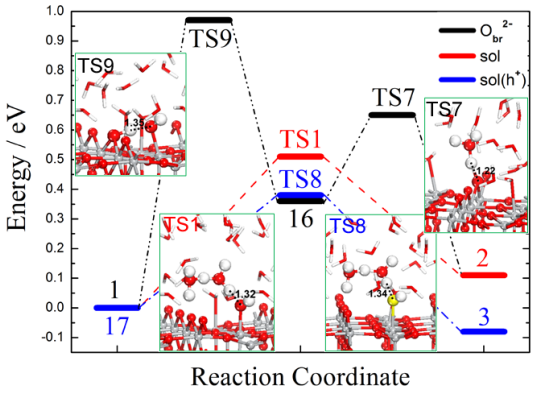

Fig. 2 | Energy profiles of possible water dissociation pathways. Three pathways are considered under aqueous surrounding at the HSE06 level, deprotonation to a nearby O_{br}^{2-} first and then into solution (black), deprotonation into solution directly (red), and deprotonation into solution with the help of a hole (blue). The TS structures are inserted with surface radicals highlighted in yellow and other related structures are shown in Supplementary Fig. 4. Length unit: Å.

Water dissociation. We first calculated the dissociation of H_2O adsorbed on the surface (H_2O_{ad}) with and also without the participation of photoholes h^+. Three possible pathways were examined as shown in Fig. 1b and Fig. 2: (i) H_2O_{ad} donates a H to a nearby bridge oxygen O_{br}^{2-} (black curve in Fig. 2), forming a terminal hydroxyl OH_t^- and an $O_{br}H^-$, which is the widely suggested mechanism[10,34]; (ii) H_2O_{ad} releases a proton directly into solution (red curve), yielding an OH_t^- and a proton in water H^+(sol); and (iii) H_2O_{ad} deprotonates (loses a proton) in the presence of h^+ (blue curve), producing an $\cdot OH_t$ radical and a H^+(sol).

It was found that in the presence of liquid water (Fig. 2 and Supplementary Table 1), pathway (i) is in fact not favored, being endothermic by 0.36 eV with a high barrier of 0.97 eV (TS9 in Fig. 2). Instead, pathway (ii) is more favored; H_2O_{ad} can deprotonate directly into solution through a Grotthuss-type proton transfer[35] with a barrier of 0.51 eV and an enthalpy change (ΔH) of 0.11 eV at neutral pH. At the transition state (TS), the detaching H^+ is bounded by water molecules, forming a Zundel-like ($H_5O_2^+$) structure (TS1 in Fig. 2). Then after a series of catch-and-abandon like proton transfer across the Grotthuss chain, it forms a stable $H_5O_2^+$ species in the bulk water and leaves an OH_t^- on the surface. Interestingly, in pathway (iii) the participation of h^+ can further lower the deprotonation barrier to 0.39 eV, and the reaction also becomes exothermic (ΔH= -0.08 eV, pH=7). At the TS, the h^+ is found to be shared by the OH group and a nearby O_{3c} (TS8 in Fig. 2 and Supplementary Fig. 5), which could facilitate the water deprotonation by weakening the $\cdot$OH-H^+ bond and stabilizing the OH adsorption structure[27]. Although pathway (iii) appears to be the most favored one, the concentration of surface-reaching holes (C_{h+}; ignoring the surface recombination) is so low in TiO_2 ($C_{h+}\approx10^{-9}$ ML)[36] that the kinetics of this concerted-like water dissociation with h^+ involved ($H_2O + h^+ \rightarrow \cdot OH_t + H^+$(sol)) is in fact less favored (Supplementary Note 3). Our kinetic modelling shows that it is about three orders of magnitude slower than the direct deprotonation

(*i.e.* pathway (ii)) followed by a hole transfer process, being consistent with the results of Chen et al. on anatase TiO_2[9].

Surface Radicals. After identifying the favored pathway of water dissociation yielding OH_t^-, we investigated the formation of surface radicals (Methods), *e.g.* $\cdot OH_t$ and O_{br}^- (Fig. 4d), which are the key species in photocatalytic OER. It was found that the hole trapping at OH_t^- ($OH_t^- + h^+ \rightarrow \cdot OH_t$) is 0.24 eV more favourable than that observed for O_{br}^{2-} ($O_{br}^{2-} + h^+ \rightarrow O_{br}^-$). Additionally, compared to the situation in the gas phase[27], it is worth noting that the absolute values of the hole trapping capacity of surface hole traps (*e.g.* OH_t^- and O_{br}^{2-}) are remarkably reduced by ~0.6 eV in the presence of liquid water. This indicates that those surface hole traps are stabilized by the surrounding water so much that they are much less prone to trap h^+. Furthermore, it is interesting to note that once the $\cdot OH_t$ radical is formed, it can readily transform into O_t^- radical on the surface via detaching a H^+ into the solution[13,37] with a barrier as low as 0.41 eV at neutral pH (TS2 in Fig. 4a and Supplementary Fig. 5). The existence of O_t^- radical is made evident in our calculated spin charge density (Fig. 4d) and the easiness of the O_t^- formation from $\cdot OH_t$ radical is in accordance with the experimental results[38].

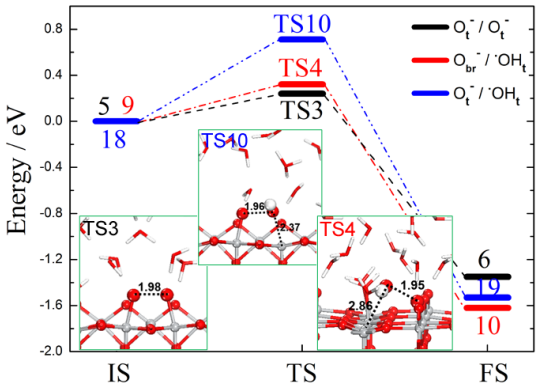

Fig. 3 | Energy profiles of OO coupling reactions among various surface radicals. Three pathways are considered under aqueous surrounding at the HSE06 level: coupling between $\cdot OH_t$ and O_{br}^- (red), $\cdot OH_t$ and O_t^- (blue), two O_t^- radicals (black). The TS structures are inserted and other related structures are shown in Supplementary Fig. 4. Length unit: Å.

OO Coupling. Regarding the second part of the mechanism, *i.e.* the coupling of the surface species, all the possible couplings were considered in the current work. We found that all the non-radical species (OH_t^- or O_{br}^{2-}) are inert for coupling with each other, even including even one non-radical coupling with one radical, due to the saturation of valence electrons. For example, the coupling barriers (E_a^{coup}) of O_t^-/O_{br}^{2-} (short for coupling between O_t^- and O_{br}^{2-}), $\cdot OH_t/O_{br}^{2-}$, and O_t^-/OH_t^- are all higher than 1.5 eV with large endothermic reaction energies of 2.55, 1.74, 1.35 eV, respectively. Thus, the only promising OO couplings reside in the pairing among surface radicals ($\cdot OH_t$, O_t^- and O_{br}^-), corresponding to total 6 possibilities: (i) O_t^-/O_t^-; (ii) $\cdot OH_t/O_t^-$; (iii) $\cdot OH_t/\cdot OH_t$; (iv) $\cdot OH_t/O_{br}^-$; (v) O_{br}^-/O_{br}^- and (vi) O_t^-/O_{br}^-, as shown in Fig. 1c.

Our DFT calculations show that the O_{br}^-/O_{br}^- pathway is not likely, owing to the infeasible thermodynamics in producing two neighboring O_{br}^- radicals. Also, neither

does the O_t^-/O_{br}^- pathway due to the relatively long distance at the TS between O_t^- and O_{br}^- with a large E_a^{coup} of ~1.0 eV. For the $\cdot OH_t/\cdot OH_t$ pathway previously proposed[4], our calculations show that the E_a^{coup} is 0.66 eV, which is higher than the deprotonation barrier of $\cdot OH_t$ radical (0.41 eV). In other words, $\cdot OH_t$ is more inclined to deprotonate into O_t^- radical rather than to couple with another adjacent $\cdot OH_t$ radical. The remaining three possible pathways are compared in Fig. 3 and Supplementary Table 2. One can see that the $\cdot OH_t/O_t^-$ pathway is not easy because of a high E_a^{coup} of 0.71 eV (TS10 in Fig. 3), while the remaining two pathways (O_t^-/O_t^- and OH_t/O_{br}^-) are both favored with the barriers of ~0.3 eV (TS3, TS4 in Fig. 3). The necessity of radicals (Supplementary Fig. 5) in the O-O bond formation from our work displays strongly the indispensable role of radicals in photo-catalytic OER. In addition, the OO coupling is generally more difficult to occur at the liquid/solid interface, compared to the case without liquid water where all the barriers are below 0.15 eV (Supplementary Table 2), demonstrating the constraint effect of H-bond network on the coupling reactions.

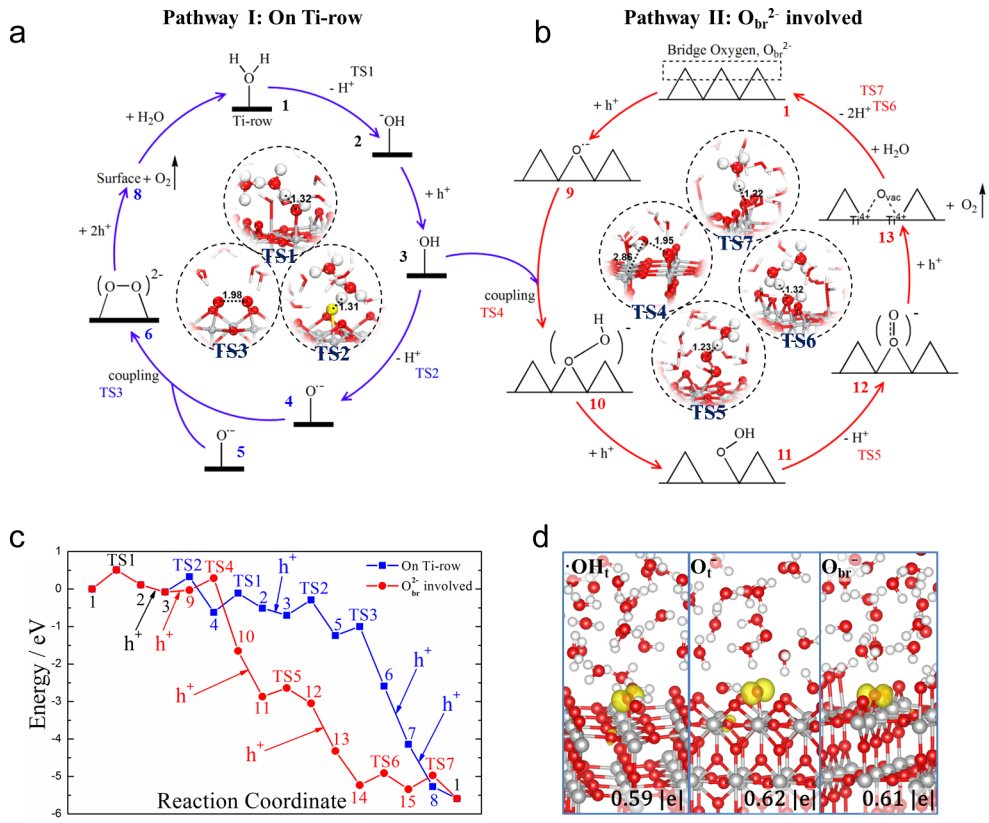

Fig. 4 | Proposed mechanism (dual pathways) and energy profiles for photocatalytic OER. **a**, One of the dual pathways (pathway I) occurring on the Ti-row. **b**, The other pathway (pathway II) involving bridge oxygen. Inserts (circles) correspond to the TS structures, and all the detailed information of the structures is shown in Supplementary Fig. 4 and 5. **c**, The energy profiles of pathways I and II, in which states 1, 2, …15 correspond to the states in (**a**) and (**b**). The elementary steps involving holes are labeled by h^+. **d**, The existence of three key surface radicals in the process. They are illustrated by the spin density plots (dumbbell-shaped O-2*p* orbital; iso-value of 0.005) and the Bader charge difference (~0.6 |e| means that it is positively charged

with +0.6 |e| with respect to the lattice O in bulk TiO_2).

The general picture of OER. Combining all the elementary steps calculated, an OER mechanism with dual pathways can be obtained as shown in Fig. 4: one of the dual pathways occurs on Ti-row sites (the blue curve, named as pathway I) and the other involves bridged oxygen (red curve; pathway II). In pathway I (Fig. 4a), it starts from the deprotonation of an adsorbed water to generate an OH_t^-, followed by the trapping of a h^+ to form a $\cdot OH_t$ on the surface. Then, the $\cdot OH_t$ deprotonates readily, yielding a O_t^- radical. After coupling with another O_t^- nearby, two successive h^+ can oxidize the as-formed $(O_t\text{-}O_t)^{2-}$ into an O_2. On the other hand, in pathway II (Fig. 4b) the $\cdot OH_t$ radical may couple with an O_{br}^- directly instead of deprotonation, and thus the lattice oxygen is involved in the OER. Then after a sequence of h^+ trapping and deprotonation, the O_2 molecule is generated and readily released, leaving an ionized oxygen vacancy (O_{vac}^{2+}) on the surface. The generated O_{vac}^{2+} can be easily filled by the adsorption of H_2O with two sequential deprotonation steps, recovering the surface. The following points should be noted: (i) Pathway II involves lattice oxygen and thus it may cause surface roughening, which will be discussed later; (ii) The requirement of two adjacent radicals for OO coupling and the successive oxidation of O_2^{2-} into O_2 in the OER mechanism indicate that the surface needs to accumulate some holes in order to effectively drive the multi-hole process, consistent with experimental results from rate law analysis[39,40]. In general, the sequential oxidation of O_2^{n-} species by h^+ ($O_2^{2-}\rightarrow O_2^-\rightarrow O_2$; Supplementary Fig. 6) is clearly accompanied by the step-by-step decrease in the bond length of O-O ($l_{O\text{-}O}$; 1.48→1.35→1.23 Å) as well as the progressively stretched $l_{Ti\text{-}O}$[41], as shown in Table 3, thus indicating the gradual detachment of an oxygen from the surface.

Kinetic analysis. Fig. 4c shows the energy profiles of these two pathways and it may appear that both pathways should be kinetically fast because of the low barriers (the highest barrier is 0.50 eV) and large energy releases (Supplementary Note 5 and 6). This is in contrast with the general consensus that the performance of TiO_2 is still very low for photocatalytic OER. How can we understand this? What is the main obstacle that limits the overall efficiency of OER on TiO_2? Having obtained the complete pathways and the energetics of elementary steps in OER, we are able to carry out the kinetic analysis utilizing micro-kinetics to address these issues quantitatively[42].

Table 2 | Reaction energetics of each elementary step for solving the kinetic modelling

Reaction equations	Steps	ΔH / eV	E_a / eV
$H_2O(sol) + * \rightarrow *OH^- + H^+(sol)$	1 → 2	0.11	0.51
$*OH^- + h^+ \rightarrow *OH\text{-}rad$	2 + h^+ → 3	-0.19	\ [a]
$*OH\text{-}rad \rightarrow *O^- + H^+(sol)$	3 → 4	-0.54	0.41
$*O^- + *O^- \rightarrow *O_2^{2-} + *$	5 → 6	-1.35	0.24
$*O_2^{2-} + h^+ \rightarrow *O_2^-$	6 + h^+ → 7	-1.55	\ [a]
$*O_2^- + h^+ \rightarrow O_2(aq) + *$	7 + h^+ → 1	-1.45	\ [a]
$^{\#}O_{br}^{2-} + h^+ \rightarrow {}^{\#}O_{br}^-$	3 + h^+ → 9	0.05	\ [a]

$^{\#}O_{br}^{-}$ + *OH-rad → $^{\#}O_{br}OH^{-}$ + *	9 → 10	-1.62	0.32
$^{\#}O_{br}OH^{-} + h^{+} \rightarrow {}^{\#}O_{br}OH$	10 + h^{+}→11	-1.22	\ [a]
$^{\#}O_{br}OH \rightarrow {}^{\#}O_{br}O^{-} + H^{+}(sol)$	11 → 12	-0.18	0.23
$^{\#}O_{br}O^{-} + h^{+} \rightarrow O_2(aq) + {}^{\#}$	12 + h^{+}→13	-1.27	\ [a]
$H_2O(sol) + {}^{\#} \rightarrow {}^{\#}H_2O$	13 → 14	-0.91	\ [a]
$^{\#}H_2O \rightarrow {}^{\#}OH^{-} + H^{+}(sol)$	14 → 15	-0.11	0.32
$^{\#}OH^{-} \rightarrow {}^{\#}O_{br}^{2-} + H^{+}(sol)$	15 → 1	-0.25	0.37

All the results are calculated using our MPA-MD method except for the hole diffusion barrier ([a] taken from ref. 48; Supplementary Note 8). Rate equations are shown in Supplementary Table 3.

We first estimated the reaction kinetics under the experimental concentration of surface-reaching holes (C_{h+} = ~10^{-9} ML) by utilizing a steady-state microkinetic model within the framework of Transition State Theory. All the considered reactions and energies are shown in Table 2, where * represents the free site of Ti_{5c} on the Ti-row while # represents the free site of O_{vac} on the O_{br}-row, corresponding to the elementary steps in Fig. 4c. The total coverage of all intermediate species adsorbed on each kind of surface site (Ti_{5c} on the Ti-row or O_{vac} on the O_{br}-row) are treated as unity, respectively. The kinetic equations are solved under the condition of χ_{H_2O} =1 (mole fraction), χ_{O_2} = 10^{-7}, pH = 7, T = 300 K. Differing from the oxygen reduction reaction ($\chi_{O_2\,(aq)} = 2.34 \cdot 10^{-5}$ corresponding to 1 atm $O_{2(g)}$ in equilibrium with $O_{2(aq)}$)[43], a relatively smaller χ_{O_2} value is used because of the extremely unsaturated situation of O_2 in water caused by the slow reaction kinetics of OER (Supplementary Note 7). More importantly, we further investigated the influences of different kinetic barriers (i.e. water dissociation, OO coupling and hole diffusion) and/or C_{h+} on the total turn-over frequency (TOF, which is a quantitative measure of the overall rate), by applying a similar approach with the method proposed by Campbell and coworkers[44] (i.e. degree of rate control). For instance, when investigating the influence of water dissociation barrier and/or C_{h+} on the total TOF, we keep the barriers of OO coupling and hole diffusion as constant, meanwhile mapping the TOF value (solve the kinetic equations at every single point) in the vertical range of (0, 1.5) for the dissociation barrier at intervals of 0.01 and in the horizontal range of (-10, 0) for the $\log_{10}C_{h+}$ at intervals of 0.1, corresponding to a mesh density of 150×100 in the figure.

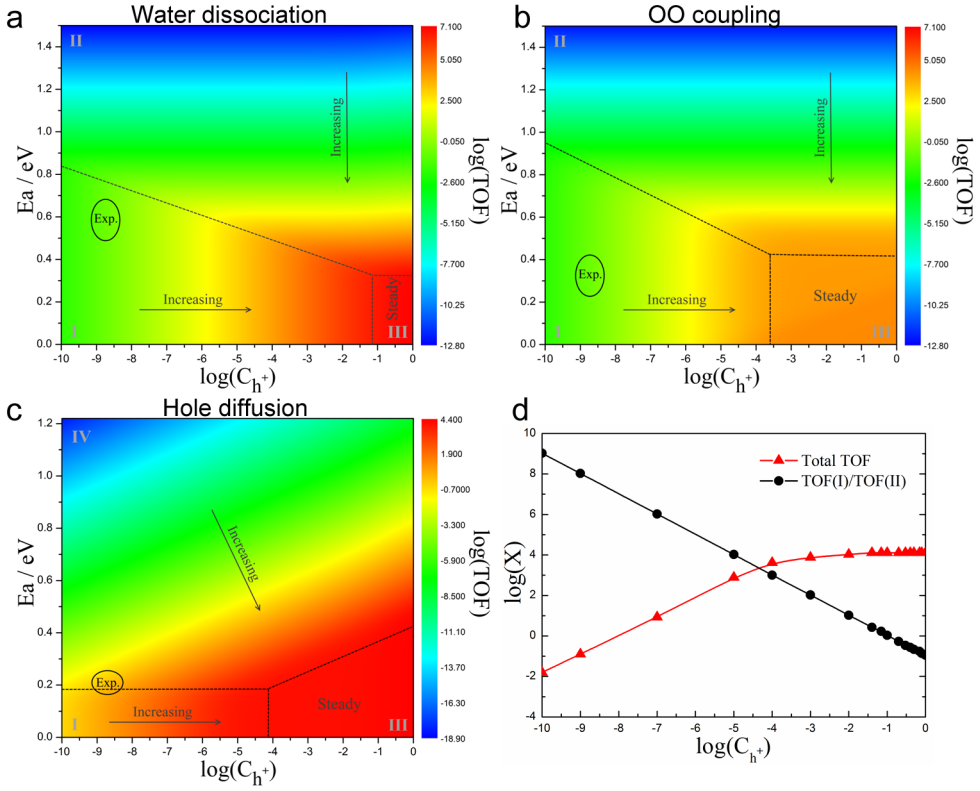

Fig. 5 | TOF as a function of the hole concentration from microkinetic analyses. a-c, Influence of different kinetic barriers (water dissociation (**a**), OO coupling (**b**) and hole diffusion (**c**)) and C_{h+} on the total TOF (Supplementary Note 7 and 8). The trends in different regions are indicated by black arrows. The experimental concentrations of holes with calculated barriers are labeled as black circles. **d**, The contribution ratio between pathways I and II to the total TOF.

Our kinetic analysis results of investigating the influence of different kinetic barriers and C_{h+} on the TOF value are shown in Fig. 5. They show that there are different regions in which the TOF is affected by (i) only C_{h+} (region I); (ii) only the barrier (region II); (iii) neither of C_{h+} nor barrier (region III); and (iv) both of C_{h+} and the barrier (region IV). Several striking features are revealed in the figure. Firstly, at the experimental concentration of surface-reaching holes (C_{h+} = ~10^{-9} ML)[36], the total TOF would be dramatically hindered, being five orders of magnitude lower compared to the case when photoholes are always available (C_{h+} = 1 ML) as shown in Fig. 5d. This explains the origin of low activity observed experimentally. Secondly, there is a considerable margin where all the reaction barriers on TiO_2 can be increased without reducing considerably the TOF considerably. For example, the water dissociation barrier can increase from 0.51 eV (the DFT value on TiO_2) to ~0.8 eV without affecting the TOF at C_{h+} = 10^{-9}. Similarly, the TOF is roughly constant if the OO coupling barrier is below 0.8 eV (the DFT value is only ~0.3 eV). This is a very surprising finding, which provides strong theoretical evidence to show that under the experimental conditions the inherent catalytic activity of TiO_2 is adequate (*i.e.* the barriers are low enough) and the main obstacle that limits the overall efficiency of

OER is in fact the low concentration of surface-reaching holes. Thirdly, lowering the barrier of water dissociation can increase the TOF once C_{h+} is higher than ~10^{-4}, shown in Fig. 5a. In other words, to further increase the TOF one must increase the catalytic activity of TiO_2 (lower the barriers), if C_{h+} is higher than ~10^{-4}. This suggestes that C_{h+} = ~10^{-4} is a critical threshold to signify whether the catalytic activity or the concentration of hole needs to be improved.

Our kinetic results also reveal that both the hole diffusion barrier (Supplementary Note 8) and C_{h+} can influence the TOF in region IV (Fig. 5c), and the diffusion barrier threshold between region I and IV is ~0.19 eV. Considering that the diffusion barrier in rutile TiO_2 is already so low[45] that it would be difficult for a further decrease. The most effective way to enhance the photocatalytic efficiency is again to increase the concentration of photoholes. Another finding of the kinetic analysis is that the two pathways possess different characteristics of hole-concentration dependence: the pathway involved lattice oxygen (pathway II) tends to reduce its contribution to the total TOF as C_{h+} is decreased, from the dominant role at C_{h+} = 1 (~89%) to a negligible one (~10^{-8}) at C_{h+} = 10^{-9} (Fig. 5d and Supplementary Table 4 and 5). This change in reaction channels/mechanism varying with C_{h+} was also found in other materials, such as hematite[40]. It may be worth noting that, despite remarkable progress made previously pointing out that the photoactivity is significantly affected by the hole concentration[39,40,46], the analysis above describes quantitatively, by virtue of microkinetic analysis, the effects of each of the kinetic components on the overall efficiency and it may be extremely difficult to obtain these quantities using other approaches.

Table 3 | Geometric properties of key species involved in the dual pathways

Items	$N_{Ti\text{-}O}$[a]	$l_{Ti\text{-}O}$[b]	$l_{O\text{-}O}$[c]	$v_{O\text{-}O}$[d]	Items	$N_{Ti\text{-}O}$[a]	$l_{Ti\text{-}O}$[b]	$l_{O\text{-}O}$[c]	$v_{O\text{-}O}$[d]
OH_t^-	1	1.83	\	\	O_{br}^{2-}	2	1.85;1.85	\	\
$\cdot OH_t$	1	2.25	\	\	O_{br}^-	2	2.06;2.06	\	\
O_t^-	1	2.00	\	\	$(O_{br}\text{-}OH)^-$	2	2.11;2.14	1.48	816
$(O_t\text{-}O_t)^{2-}$	2	1.97;2.00	1.46	840	$(O_{br}\text{-}OH)$	1	2.37	1.34	1145
$(O_t\text{-}O_t)^-$	1	2.25	1.34	1108	$(O\text{-}O_{br})^-$	2	2.26;2.38	1.35	1115
$(O_t\text{-}OH)^-$	1	2.00	1.47	928	O_2 (aq)	0	\	1.23	1492

All the results are calculated in the presence of aqueous solution, including: [a] number of Ti-O bonds, bond length of [b]Ti-O and [c]O-O bonds (unit: Å), and [d]stretching frequency (wavenumber: cm^{-1}) of O-O bonds.

Insights into the diverse experimental observations. Having performed the kinetic analysis, we are now at the position to rationalize some classical but puzzling experimental observations. Firstly, it was detected that on rutile TiO_2 there are three characteristic MIR-IR (multiple internal reflection infrared radiation) signals[5]: 838 cm^{-1}, 812 cm^{-1} and 928 cm^{-1}. More interestingly, a change of peak intensity under different pH was observed: when switching from acid (pH 2.4) to alkaline (pH 11.9) solutions, the peak of 812 cm^{-1} increases while the peak of 928 cm^{-1} decreases. However, what surface species are responsible for these signals and why the two peak

intensities shift are still elusive. The current work can shed some lights on these issues: Our simulated stretching frequencies of key O-O species (Methods) are listed in Table 3, which shows that the three frequencies of 840 cm^{-1}, 816 cm^{-1} and 928 cm^{-1} agree well with the experimental signals, identifying the corresponding species (i.e. $(O_t\text{-}O_t)^{2-}$, $(O_{br}\text{-}OH)^-$ and $(O_t\text{-}OH)^-$, respectively) for these signals. Besides, the peak intensity changes can be understood by taking the pH dependence of the concentrations of surface radicals into account. For instance, the peak growth of 812 cm^{-1} (corresponding to $(O_{br}\text{-}OH)^-$), is attributed to the rise of O_{br}^- concentration as pH increases: Increasing the pH from 2.4 to 11.9 would enlarge the concentration of O_{br}^{2-} which is easily oxidized by h^+ to form O_{br}^-, and further promote the $O_{br}^-/\cdot OH_t$ coupling, leading to an increase of $(O_{br}\text{-}OH)^-$. The peak intensity change of 928 cm^{-1} can be explained in a similar way.

Secondly, we can rationalize the well-known observation of a sharp decrease of photoluminescence (PL) intensity[8] around pH 4: the availability of surface O_{br}^{2-} increases as pH goes above 4.3[47], thus facilitating the pathway involving the lattice oxygen and greatly suppressing the recombination of photo-induced carriers. As pH is further increased, all the deprotonation steps are promoted, corresponding to the further decrease of PL intensity, which even approaches to zero near pH 13. Thirdly, another experimental observation whereby the surface roughening on rutile (110) was significantly suppressed at pH 13 compared to pH 1.1[8] can also be understood by our findings: O_{br}^- radical can only couple with $\cdot OH_t$ instead of O_t^-, and thus the lack of $\cdot OH_t$ in strong alkaline solution reduces the possibility of $O_{br}^-/\cdot OH_t$ coupling, leading to the decrease in the rate of pathway II and hence a reduction of surface roughening. Similarly, our result showing that pathway II becomes favored if C_{h+} is high can explain the experimental fact that low-intensity UV illumination causes little surface roughening on rutile (110), and it becomes more prominent with the increasing illumination intensity (from 0.04 to 50 mW/cm^2)[7]. All these results strongly support our proposed mechanism.

Discussion

It is worth discussing some implications of our results in photo-catalytic water splitting: In photocatalytic OER, the radicals are perhaps the most important intermediates; however, in which manner they play this essential role has remained elusive. This fundamental question can be answered as follows. Firstly, radicals can reduce the Ti-O bonding strength in accordance with the stretched $l_{Ti\text{-}O}$ of radicals as shown in Table 3, and thus could facilitate the desorption of O_2. For instance, the oxygen vacancy formation energy of O_{br}^{2-} (the normal bridge oxygen) and O_{br}^- (the bridge oxygen radical) were calculated to be 3.16 eV and 1.54 eV, respectively, which clearly reveals the contributions of radicals in promoting the removal of lattice oxygen. Secondly, they are irreplaceable intermediates for OO coupling where non-radical species are inert. In particular, it is worth mentioning the specific role of $\cdot OH_t$ radical in the process. As mentioned before, the favored OO coupling on Ti-row is between two O_t^- radicals, and hence the difficulty in producing O_t^- largely decides the feasibility of this pathway. However, the direct deprotonation of OH_t^- can

hardly occur due to the fast reverse reaction with a very low barrier of 0.08 eV. Therefore, the only way is to trap a h^+ and form $\cdot OH_t$ first, followed by the deprotonation of $\cdot OH_t$ into the O_t^- radical. In other words, the ease of deprotonation of $\cdot OH_t$ influences the main pathway of OER under experimental conditions. Thirdly, they are actually trapped holes on the surface, which can significantly suppress the surface electron-hole recombination and increase the lifetime of surface-reaching holes up to microseconds[48,49].

Here, we develop a first principles MPA-MD method to extensively simulate the OER in the presence of liquid water on rutile TiO_2(110). A complete reaction mechanism with dual pathways is identified, which allow us to join some detached experimental observations and to rationalize the experimental results. Moreover, we provide strong theoretical evidence to show that the low efficiency of OER on TiO_2(110) is in fact not limited by the inherent catalytic activity (reaction barriers), but by the low concentration of photoholes on TiO_2. Perhaps the low concentration of surface-reaching photoholes may be a general obstacle in many other materials [18]. In addition, this finding also explains that rutile TiO_2 is a very good coating material for the photoanode in protecting the effective but unstable light-harvesting semiconductors from corrosion by virtue of its high kinetic activity, stable structure and transparent property[50]. It is clear that the most efficient way to improve the performance of OER at the current stage (before approaching the estimated threshold of $C_{h^+} = \sim 10^{-4}$) is to enrich the concentration of surface-reaching photoholes rather than to lower the reaction barriers of water dissociation and OO coupling. The following two strategies derived from the current work may reach this goal in addition to conventional methods; the one is to lower the hole diffusion barrier; and the other is to reduce the hole diffusion distance, *i.e.* achieving surface or near-surface photoexcitation.

Methods

DFT calculations. All the spin-polarized calculations were performed with Perdew-Burke-Ernzerhof (PBE) functional using the VASP code[51,52]. The project-augmented wave (PAW) method was used to represent the core-valence electron interaction with electrons from Ti 3*p*, 3*d*, 4*s*; O 2*s*, 2*p*; and H 1*s* shells explicitly included. The valence electronic states were expanded in plane wave basis sets with energy cutoff of 450 eV, and the occupancy of the one-electron states was calculated using the Gaussian smearing with SIGMA = 0.05 eV. The ionic degrees of freedom were relaxed using the BFGS minimization scheme until the Hellman-Feynman forces on each ion were less than 0.05 eV/Å. The transition states were searched using a constrained optimization scheme, and were verified when (i) all forces on atoms vanish; and (ii) the total energy is a maximum along the reaction coordinate but a minimum with respect to the rest of the degrees of freedom. The force threshold for the TS search was 0.05 eV/Å. The dipole correction was performed throughout the calculations to take the polarization effect into account.

Regarding the calculation on the stretching frequency of O-O bonds: firstly, we

fully optimized the structures (with water solution included) until the force on each atom is less than 0.01 eV/Å. Then, we fixed all the atoms except the relevant O atoms, and calculated the stretching frequency of each O-O bond by setting IBRION = 5. It should be noted that in calculating the frequency a very small movement (POTIM = 0.001) but a very high convergence criteria (EDIFFG = $1E^{-6}$) are necessarily applied. Finally, six frequencies located in different wavenumber ranges for each structure are obtained, and only the frequency values in the experimental detection range are listed in Table 3.

Molecular dynamics (MD) simulations. The MD calculation was performed using a four-Ti-layer *p*(1×4) periodical rutile (110) slab with a ~15Å vacuum between slabs, and a corresponding 1×2×1 K-points mesh was used during optimizations. A lattice matching bulk ice (containing 26 H_2O) was introduced above the surface as an initial aqueous network (with a density similar with liquid water) at the liquid-solid interface. The simulation temperature was set at 300K (experimental temperature) with a 0.5 fs movement for each step in the canonical (NVT) ensemble employing Nosé–Hoover thermostats. For the MD simulation of each IMS (~9 ps), we found that the water structures in our systems often change significantly in the first ~2 ps, and reach quasi-equilibrium around 3 ps, as indicated by the black arrow in Supplementary Fig. 2, taking the MD simulation for water/TiO_2(110) interface structure as an example. Then we ran MD for a period of ~6 ps to confirm that the systems were in equilibrium. The structures of the input ice-like water and the water structure after the MD are shown as the inserts. One can see that the initial ice-like structure has perfectly repeated six-member ring structure in the water layer, but lacks of close interaction with the TiO_2 surface. However, the water layer after the MD is relatively less structured with distorted six-, five-, or four-member ring structures, but the water/TiO_2 interface is well constructed with enriched density of H atoms as demonstrated by the radial distribution graph in Fig. 1a.

Constrained MD. The constrained MD method was well established on the basis of thermodynamic integration of the free energy gradient[53-55]. It is a well accepted approach to calculate the free energy change (including reaction barriers). Taking the O_2 dissociation reaction on Pt(111) as an example (reaction 3 in Table 1; Supplementary Fig. 3), the O-O bond distance is stretched gradually from 1.4 to 2.1 Å. For each point per 0.1 Å, we performed *ab initio* MD simulations at a constant temperature (T = 300 K) until the interatomic force between the two constrained atoms (i.e. O···O) were converged. All the interatomic forces along the reaction coordinate, which are the corresponding free energy gradients, can be readily obtained. Then by integrating the free energy gradients, the free energy change can be computed. In Supplementary Fig. 3, one can see that the highest point in the free energy profile is located at the O-O distance of 2.0 Å, corresponding to the transition state of O_2 dissociation with the barrier of 0.39 eV.

Localization of photoholes. The localization of a hole on a particular O site of TiO_2

can be obtained by structure optimizations using the BFGS optimization method. Initial magnetic moments on each atom are usually necessary in the input setting, although they will be optimized during the calculation. In order to ensure the electro-neutrality of the system and eliminate the possibly incorrect energy result from the background charge, trapped holes or surface radicals were simulated by introducing an OH group on the opposite surface instead of extracting electrons out of system in this study[27]. Besides, the on-site Hubbard U term (DFT+U) was added on O 2*p* orbitals at the value of 6.3 eV (usually ranging from 3.0 to 7.0 eV) throughout all the MD simulations to hold the spin-polarized property of trapped holes or surface radicals. We further did HSE06 corrections on all the selected samples from each MD simulation with the electronic minimization algorithm specified to the Damped method and a very soft augmentation charge (PRECFOCK = Fast).

The radical species possess distinctive features relative to their non-radical charged species, and we can distinguish them easily from the following. (i) Magnetic signals: Pure TiO_2 slab has no spin-polarizing features (mag = 0) and the generation of radical species always introduces obvious magnetic signals in the spin-polarized calculation output file (mag = 1). (ii) Geometry structures: The hole localization (generation of radicals) is accompanied with the distinct elongations of Ti-O bonds by the outward movement of the lattice Ti^{4+} ions. We have discussed this aspect in our previous work systematically[27]. (iii) Electronic structure analysis: The localization of the hole can be further confirmed by the electronic structure analysis of site-projected magnetic moments (~0.8 μ_e) and the Bader charge difference (~ 0.6 |e|; positively charged with +0.6 |e| compared to the lattice O in bulk TiO_2). We have done electronic analysis on all the hole related calculations as visualized by the spin density plots (Supplementary Fig. 5).

Data availability. All data are available within the article (and its Supplementary Information files) and from the corresponding authors upon reasonable request.

References

1 Chen, X., Shen, S., Guo, L. & Mao, S. S. Semiconductor-based photocatalytic hydrogen generation. *Chem. Rev.* **110**, 6503-6570 (2010).

2 Thompson, T. L. & Yates, J. T., Jr. Surface science studies of the photoactivation of TiO_2-new photochemical processes. *Chem. Rev.* **106**, 4428-4453 (2006).

3 Nozik, A. J. Photoelectrolysis of water using semiconducting TiO_2 crystals. *Nature* **257**, 383-386 (1975).

4 Salvador, P. & Decker, F. On the generation of H_2O_2 during water photoelectrolysis at n-TiO_2. *J. Phys. Chem.* **88**, 6116-6120 (1984).

5 Nakamura, R. & Nakato, Y. Primary intermediates of oxygen photoevolution reaction on TiO_2 (Rutile) particles, revealed by in situ FTIR absorption and photoluminescence measurements. *J. Am. Chem. Soc.* **126**, 1290-1298 (2004).

6 Cai, R. X., Kubota, Y. & Fujishima, A. Effect of copper ions on the formation of hydrogen peroxide from photocatalytic titanium dioxide particles. *J. Catal.* **219**, 214-218 (2003).

7 Nakamura, R., Okamura, T., Ohashi, N., Imanishi, A. & Nakato, Y. Molecular mechanisms of

photoinduced oxygen evolution, PL emission, and surface roughening at atomically smooth (110) and (100) n-TiO_2 (rutile) surfaces in aqueous acidic solutions. *J. Am. Chem. Soc.* **127**, 12975-12983 (2005).

8 Imanishi, A., Okamura, T., Ohashi, N., Nakamura, R. & Nakato, Y. Mechanism of water photooxidation reaction at atomically flat TiO_2 (rutile) (110) and (100) surfaces: dependence on solution pH. *J. Am. Chem. Soc.* **129**, 11569-11578 (2007).

9 Chen, J., Li, Y. F., Sit, P. & Selloni, A. Chemical dynamics of the first proton-coupled electron transfer of water oxidation on TiO_2 anatase. *J. Am. Chem. Soc.* **135**, 18774-18777 (2013).

10 Zhao, W. N. & Liu, Z. P. Mechanism and active site of photocatalytic water splitting on titania in aqueous surroundings. *Chem. Sci.* **5**, 2256-2264 (2014).

11 Li, Y. F., Liu, Z. P., Liu, L. & Gao, W. Mechanism and activity of photocatalytic oxygen evolution on titania anatase in aqueous surroundings. *J. Am. Chem. Soc.* **132**, 13008-13015 (2010).

12 Valdés, Á., Qu, Z. W., Kroes, G. J., Rossmeisl, J. & Nørskov, J. K. Oxidation and photo-oxidation of water on TiO_2 surface. *J. Phys. Chem. C* **112**, 9872-9879 (2008).

13 Cheng, J., Liu, X., Kattirtzi, J. A., VandeVondele, J. & Sprik, M. Aligning electronic and protonic energy levels of proton-coupled electron transfer in water oxidation on aqueous TiO_2. *Angew. Chem. Int. Ed.* **53**, 12046-12050 (2014).

14 Cho, I. S. *et al.* Codoping titanium dioxide nanowires with tungsten and carbon for enhanced photoelectrochemical performance. *Nat. Commun.* **4**, 1723 (2013).

15 Gai, Y., Li, J., Li, S. S., Xia, J. B. & Wei, S. H. Design of narrow-gap TiO_2: a passivated codoping approach for enhanced photoelectrochemical activity. *Phys. Rev. Lett.* **102**, 036402 (2009).

16 Asahi, R., Morikawa, T., Ohwaki, T., Aoki, K. & Taga, Y. Visible-light photocatalysis in nitrogen-doped titanium oxides. *Science* **293**, 269-271 (2001).

17 Zhang, J., Xu, Q., Feng, Z., Li, M. & Li, C. Importance of the relationship between surface phases and photocatalytic activity of TiO_2. *Angew. Chem. Int. Ed.* **47**, 1766-1769 (2008).

18 Wang, X. *et al.* Photocatalytic overall water splitting promoted by an alpha-beta phase junction on Ga_2O_3. *Angew. Chem. Int. Ed.* **51**, 13089-13092 (2012).

19 Zhao, W.-N., Zhu, S.-C., Li, Y.-F. & Liu, Z.-P. Three-phase junction for modulating electron-hole migration in anatase–rutile photocatalysts. *Chem. Sci.* **6**, 3483-3494 (2015).

20 Schaub, R. *et al.* Oxygen vacancies as active sites for water dissociation on rutile TiO_2(110). *Phys. Rev. Lett.* **87**, 266104 (2001).

21 Aschauer, U. *et al.* Influence of subsurface defects on the surface reactivity of TiO_2: water on anatase (101). *J. Phys. Chem. C* **114**, 1278-1284 (2010).

22 Maeda, K. Direct splitting of pure water into hydrogen and oxygen using rutile titania powder as a photocatalyst. *Chem. Commun.* **49**, 8404-8406 (2013).

23 Abe, R., Sayama, K. & Sugihara, H. Development of new photocatalytic water splitting into H_2 and O_2 using two different semiconductor photocatalysts and a shuttle redox mediator IO_3^-/I^-. *J. Phys. Chem. B* **109**, 16052-16061 (2005).

24 Zhang, H., Chen, G. & Bahnemann, D. W. Photoelectrocatalytic materials for environmental applications. *J. Mater. Chem.* **19**, 5089 (2009).

25 Kafizas, A., Carmalt, C. J. & Parkin, I. P. Does a photocatalytic synergy in an anatase-rutile TiO_2 composite thin-film exist? *Chem Eur J* **18**, 13048-13058 (2012).

26 Cheng, J., Sulpizi, M., VandeVondele, J. & Sprik, M. Hole localization and thermochemistry of oxidative dehydrogenation of aqueous rutile TiO_2(110). *Chemcatchem* **4**, 636-640 (2012).

27 Wang, D., Wang, H. & Hu, P. Identifying the distinct features of geometric structures for hole trapping to generate radicals on rutile TiO_2(110) in photooxidation using density functional theory calculations with hybrid functional. *Phys. Chem. Chem. Phys.* **17**, 1549-1555 (2015).

28 Wang, D., Liu, Z.-P. & Yang, W. Proton Promoted Electron Transfer in Photocatalysis: Key Step for Photocatalytic Hydrogen Evolution on Metal/Titania Composites. *ACS Catal.* **7**, 2744-2752 (2017).

29 Wood, B. C., Schwegler, E., Choi, W. I. & Ogitsu, T. Hydrogen-bond dynamics of water at the interface with InP/GaP(001) and the implications for photoelectrochemistry. *J. Am. Chem. Soc.* **135**, 15774-15783 (2013).

30 Wood, B. C., Schwegler, E., Choi, W. I. & Ogitsu, T. Surface Chemistry of GaP(001) and InP(001) in Contact with Water. *J. Phys. Chem. C* **118**, 1062-1070 (2014).

31 Song, T. & Hu, P. Insight into the solvent effect: A density functional theory study of cisplatin hydrolysis. *J. Chem. Phys.* **125**, 091101 (2006).

32 Liu, L. M., Laio, A. & Michaelides, A. Initial stages of salt crystal dissolution determined with ab initio molecular dynamics. *Phys. Chem. Chem. Phys.* **13**, 13162-13166 (2011).

33 Bullard, J. W. & Cima, M. J. Orientation dependence of the isoelectric point of TiO_2 (rutile) surfaces. *Langmuir* **22**, 10264-10271 (2006).

34 Sun, C. H., Liu, L. M., Selloni, A., Lu, G. Q. & Smith, S. C. Titania-water interactions: a review of theoretical studies. *J. Mater. Chem.* **20**, 10319-10334 (2010).

35 Marx, D. Proton transfer 200 years after von Grotthuss: insights from ab initio simulations. *Chemphyschem* **7**, 1848-1870 (2006).

36 Thompson, T. L. & Yates, J. T. Monitoring hole trapping in photoexcited TiO_2(110) using a surface photoreaction. *J. Phys. Chem. B* **109**, 18230-18236 (2005).

37 Cheng, J., VandeVondele, J. & Sprik, M. Identifying trapped electronic holes at the aqueous TiO_2 interface. *J. Phys. Chem. C* **118**, 5437-5444 (2014).

38 Micic, O. I., Zhang, Y., Cromack, K. R., Trifunac, A. D. & Thurnauer, M. C. Trapped holes on titania colloids studied by electron paramagnetic resonance. *J. Phys. Chem.* **97**, 7277-7283 (1993).

39 Kafizas, A. *et al.* Water Oxidation Kinetics of Accumulated Holes on the Surface of a TiO_2 Photoanode: A Rate Law Analysis. *ACS Catal.* **7**, 4896-4903 (2017).

40 Le Formal, F. *et al.* Rate law analysis of water oxidation on a hematite surface. *J. Am. Chem. Soc.* **137**, 6629-6637 (2015).

41 Li, Y. F. & Selloni, A. Theoretical study of interfacial electron transfer from reduced anatase TiO_2(101) to adsorbed O_2. *J. Am. Chem. Soc.* **135**, 9195-9199 (2013).

42 Wang, D., Jiang, J., Wang, H.-F. & Hu, P. Revealing the volcano-shaped activity trend of triiodide reduction reaction: A DFT study coupled with microkinetic analysis. *ACS Catal.* **6**, 733-741 (2015).

43 Hansen, H. A., Viswanathan, V. & Nørskov, J. K. Unifying kinetic and thermodynamic analysis of $2e^-$ and $4e^-$ reduction of oxygen on metal surfaces. *J. Phys. Chem. C* **118**, 6706-6718 (2014).

44 Stegelmann, C., Andreasen, A. & Campbell, C. T. Degree of rate control: how much the energies of intermediates and transition states control rates. *J. Am. Chem. Soc.* **131**, 8077-8082

(2009).

45 Deskins, N. A. & Dupuis, M. Intrinsic hole migration rates in TiO_2 from density functional theory. *J. Phys. Chem. C* **113**, 346-358 (2009).

46 Migani, A. & Blancafort, L. What Controls Photocatalytic Water Oxidation on Rutile TiO_2(110) under Ultra-High-Vacuum Conditions? *J. Am. Chem. Soc.* **139**, 11845-11856 (2017).

47 Connor, P. A., Dobson, K. D. & McQuillan, A. J. Infrared spectroscopy of the TiO_2/aqueous solution interface. *Langmuir* **15**, 2402-2408 (1999).

48 Tamaki, Y. *et al.* Dynamics of efficient electron-hole separation in TiO_2 nanoparticles revealed by femtosecond transient absorption spectroscopy under the weak-excitation condition. *Phys. Chem. Chem. Phys.* **9**, 1453-1460 (2007).

49 Rothenberger, G., Moser, J., Gratzel, M., Serpone, N. & Sharma, D. K. Charge carrier trapping and recombination dynamics in small semiconductor particles. *J. Am. Chem. Soc.* **107**, 8054-8059 (1985).

50 Hu, S. *et al.* Amorphous TiO_2 coatings stabilize Si, GaAs, and GaP photoanodes for efficient water oxidation. *Science* **344**, 1005-1009 (2014).

51 Kresse, G. & Furthmüller, J. Efficiency of ab-initio total energy calculations for metals and semiconductors using a plane-wave basis set. *Comp. Mater. Sci.* **6**, 15-50 (1996).

52 Kresse, G. & Hafner, J. Ab initiomolecular-dynamics simulation of the liquid-metal–amorphous-semiconductor transition in germanium. *Phys. Rev. B* **49**, 14251-14269 (1994).

53 Sprik, M. & Ciccotti, G. Free energy from constrained molecular dynamics. *J. Chem. Phys.* **109**, 7737 (1998).

54 Carloni, P., Sprik, M. & Andreoni, W. Key steps of thecis-Platin-DNA interaction: density functional theory-based molecular dynamics simulations. *J. Phys. Chem. B* **104**, 823-835 (2000).

55 Bucko, T. Ab initio calculations of free-energy reaction barriers. *J. Phys. Condens. Matter.* **20**, 064211 (2008).

Acknowledgments: D.W. thanks the Chinese Scholarship Council for the abroad living support and P.H. thanks the Chinese Government for the "Thousands Talents" program. **Funding:** This work was financially supported by National Natural Science Foundation of China (21333003, 21421004, 21622305), Young Elite Scientist Sponsorship Program by CAST (YESS20150131), The Shanghai ShuGuang project (17SG30), and the Fundamental Research Funds for the Central Universities (WJ616007)

Author contributions: P.H. and H.F.W conceived the project and contributed to the design of the calculations and analyses of the data. D.W. carried out most of the calculations and wrote the first draft of the paper. T.S. and D.W. conducted the tests of the MPA-MD method. J.F.C. wrote the kinetic code and contributed to the analyses of data. All the authors discussed the results and commented on the manuscript. D.W. and T.S. contribute equally to this work.

Competing interests: The authors declare that they have no competing interests.

Additional information

Supplementary information is available for this paper at

Reprints and permissions information is available at www.nature.com/reprints .

Correspondence and requests for materials should be addressed to H.F.W. or P.H.

Publisher's note: Springer Nature remains neutral with regard to jurisdictional claims in published maps and institutional affiliations.

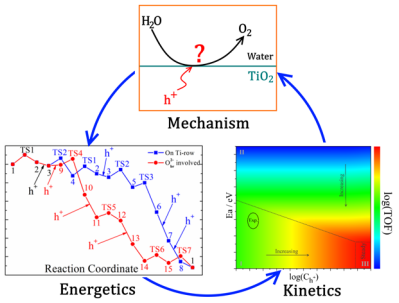

For Table of contents only